

Electromagnetic Target Detection in Uncertain Media: Time-Reversal and Minimum-Variance Algorithms

Dehong Liu, *Member, IEEE*, Jeffrey Krolik, *Member, IEEE*, and Lawrence Carin, *Fellow, IEEE*

Abstract—An experimental study is performed on imaging targets that are situated in a highly scattering environment, employing electromagnetic time-reversal methods. A particular focus is placed on performance when the electrical properties of the background environment (medium) are uncertain. It is assumed that the (unknown) medium characteristic of the scattered fields represents one sample from an underlying random process, with this random process representing our uncertainty in the media properties associated with the scattering measurement. While the specific Green's function associated with the scattered fields is unknown, we assume access to an ensemble of Green's functions sampled from the aforementioned distribution. This ensemble of Green's functions may be used in several ways to mitigate uncertainty in the true Green's function. Specifically, when performing time-reversal imaging, we consider a Green's function as a representative of the average of the ensemble, as well as Green's functions based on a principal components analysis of the ensemble. We also develop a wideband minimum-variance beamformer with environment perturbation constraints, in which the unknown Green's function is constrained to reside in a subspace spanned by the Green's function ensemble. These algorithms are examined using electromagnetic scattering data measured in a canonical set of laboratory experiments. The qualitative performance of the different techniques is presented in the form of images, with quantitative results presented in the form of receiver operating characteristic performance.

Index Terms—Electromagnetic scattering, target detection, time-reversal imaging, uncertain media.

I. INTRODUCTION

TIME reversal is a technique that exploits the multipath characteristic of complex media. Specifically, assume a source emits a pulse of energy into a complex multiscattering environment and that the propagated energy is observed on a finite set of receiving antennas. The multipath phenomenon causes a temporally localized excitation to be temporally extended as viewed at the receiver antennas, with the signals arriving later in time, having traveled a longer distance than the corresponding early arrivals. If the time-domain signals are time reversed and coherently reradiated from the antenna array, the signals arrive coherently at the original source location, approximately reconstructing the original source [1]–[4].

Manuscript received August 14, 2006; revised November 13, 2006.

The authors are with the Department of Electrical and Computer Engineering, Duke University, Durham, NC 27708-0291 USA.

Color versions of one or more of the figures in this paper are available online at <http://ieeexplore.ieee.org>.

Digital Object Identifier 10.1109/TGRS.2006.890411

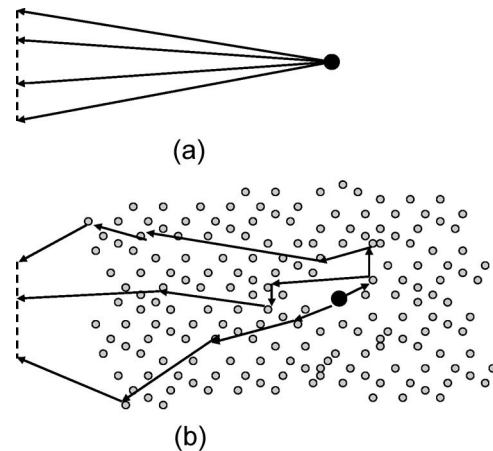


Fig. 1. Wavefronts emitted from a source, observed at a linear antenna array (at left). (a) Source in a homogeneous medium and (b) in a highly multipath environment.

In the above discussion, the time-reversed fields were assumed to be *physically* reradiated into the original domain, but this process may also be performed computationally, with an approximate medium Green's function, thereby providing the opportunity to perform imaging. Moreover, the above discussion considered imaging as a localized *source*; in the work presented here, we are interested in imaging a *target* based on the scattered fields, for which the problem complexity is heightened by the need to consider the two-way Green's function (from the source to the target and from the target to the receivers).

Time reversal has important implications for imaging and detecting targets situated in a complex medium. For example, in conventional imaging, the focusing resolution is limited by the size of the sensor-array aperture. However, time-reversal imaging may have an effective aperture [4] much larger than that of the physical array, especially in a complex highly scattering medium. Interestingly, the more complex the media are, the more propagation paths are manifested from a source to the receiver array, improving focusing quality (see Fig. 1). From this viewpoint, when we try to image targets situated in a complex environment for which conventional methods like synthetic aperture radar (SAR) may yield poor imaging quality due to the highly scattering medium, time reversal may achieve superresolved images even with a small physical array [5]–[9]. However, this superresolution property is based on the assumption that the Green's function used in time-reversal

imaging is the same as that associated with the scattered fields, with this assumption difficult to meet in practice.

Specifically, when performing time-reversal imaging, for which time reversal of the measured scattered fields is performed with a numerical model, one must address the inevitable differences between the true Green's function characteristic of the scattered fields and the simulated Green's function employed when imaging. The refocusing performance of the time-reversal technique degrades when the medium through which time-reversal imaging is performed is different from that corresponding to the actual physical measurement [10], [11]. Work addressing target detection in changing or uncertain environments has been carried out experimentally and theoretically with acoustic waves in random ocean channels for underwater target detection, termed matched-field processing (MFP) [12], [13]. In particular, the minimum-variance beamformer with environment perturbation constraints (MV-EPC) [10] is a well-known algorithm that seeks to improve imaging robustness in the presence of an uncertain sound-speed profile. This algorithm has been demonstrated to be effective in multiple experiments in imaging underwater targets using a large aperture array with narrowband acoustic waves. The analogy between MFP and time reversal provides useful guidance for robust time-reversal imaging in a changing environment. For example, in [14]–[18], time-reversal refocusing quality is examined in an ocean channel, as the acoustic medium changed with time.

Our objective in this paper is to image and detect targets situated in a highly scattering environment using electromagnetic time-reversal (ETR)-based techniques. We emphasize that, when performing imaging, we do not perform physical time reversal, in which the scattered fields are time reversed and experimentally reradiated into the domain. In imaging, this latter process is performed with a computational model, and the focus of this paper is on how strongly the image quality depends on requiring knowledge of the true underlying Green's function. We place a particular focus on performance when a small antenna aperture is employed; in addition, we consider cases for which the true media characteristic of the scattered fields is uncertain. If one does not know the precise Green's function of the media under test, other information must be exploited to obtain useful imaging results. We treat the background Green's function as a random process, with the true (unknown) Green's function representing one sample from the random process. While the true Green's function is unknown, we assume access to an ensemble of Green's functions, these representing multiple realizations of the underlying random process. The ensemble of Green's functions may now be exploited when performing inversion. For example, one may use the average of the ensemble as the Green's function in numerical time-reversal imaging, or alternatively one may employ a principal components analysis (PCA) [19], with the principal eigen-Green's functions used in time-reversal imaging. We consider these approaches, as well as a wideband extension of MV-EPC [10]. The MV-EPC algorithm performs imaging based on a constrained optimization, with the constraint based on the idea that the actual Green's function must reside in the subspace spanned by the aforementioned ensemble of Green's functions.

We extend the MV-EPC to situations of interest in wideband time-reversal imaging (previous MV-EPC work assumed large apertures and narrowband signals [10]).

The imaging algorithms are examined based on a controlled set of electromagnetic scattering measurements. Specifically, we consider quasi-2-D experiments, with the complex propagation media composed of a closely packed set of 680 randomly distributed dielectric rods. The different realizations of the random media are constituted by redistributing the positions of the rods. The measured scattered fields are performed for a target placed within one such media, with the ensemble of the Green's functions corresponding to distinct (but statistically related) rod placements. The analysis is simplified by the fact that these 2-D measurements yield an analysis with scalar fields; the techniques presented here may be, in principle, extended to the vector case, with appropriate antenna measurements required for the measurement of the vector Green's functions.

The remainder of the paper is organized as follows. A brief review of the time-reversal basics is provided in Section II, with a discussion of the literature for time reversal applied to situations of uncertain (or changing) media. In Section III, techniques are described for performing time-reversal imaging in uncertain environments, and in Section IV, we describe the experimental system used for algorithm evaluation. Example imaging results are presented in Section V, followed by the conclusion in Section VI.

II. THEORY OF TIME REVERSAL IN CHANGING MEDIA

Researchers have theoretically investigated time-reversal imaging quality when there is a mismatch between the true Green's function characteristic of the scattered fields and the Green's function used when performing time reversal. In this previous research [20], it was assumed that the observed fields were manifested from a source (i.e., the scattering problem was not considered); we review this literature, to motivate the imaging techniques considered for the scattering problem, when the true Green's function is uncertain.

Time reversal of a source in the frequency domain is the product of two Green's function (here considering the problem of source localization). The first one sends the signal from the source to the array of detectors, and the second one back-propagates the signal from the detector array. For the case of different Green's functions in the forward and inverse phases, the product of operators has a kernel represented by the correlation function of the two corresponding Green's functions. In the Lippman–Schwinger representation of the wave equation [21], the correlation of the two Green's functions is proportional to the power spectrum of the random heterogeneities of the underlying heterogeneous media. If we denote by $\delta c(\mathbf{x})$ the fluctuations in the propagation speed of the underlying medium relative to a reference homogeneous medium, the correlation function as a function of position \mathbf{x} is defined by $R(\mathbf{x}) = \langle \delta c(\mathbf{y}) \delta c(\mathbf{x} + \mathbf{y}) \rangle$, which is independent of \mathbf{y} when the fluctuations are statistically independent by translation. The power spectrum $\hat{R}(\mathbf{k})$ is defined as the Fourier transform of the above correlation.

When the underlying medium does not change between the two phases of the time-reversal experiment, it is well known that the correlation of the two Green's function solves a radiative transfer equation in the phase space [21]. When the two media are different, then the radiative transfer equation must be modified. The salient feature of this modification is the following: the scattering coefficient in the radiative transfer equation, which was proportional to the power spectrum of the heterogeneities, is now proportional to the cross correlation of the two sets of heterogeneous fluctuations (see [20]). When $\delta c_j(\mathbf{x})$ are the speed fluctuations during states $j = 1$ (forward stage) and $j = 2$ (backward stage) of the time-reversal experiment, the cross correlation is given by $R_{12}(\mathbf{x}) = \langle \delta c_1(\mathbf{y}) \delta c_2(\mathbf{x} + \mathbf{y}) \rangle$.

The analysis by the study in [22] shows that the intensity of the time-reversed signal is all the more important when the medium is scattering, i.e., heterogeneous. Consequently, when the two random media become less correlated, the scattering term in the radiative transfer equations decreases and so does the intensity of the time-reversed signal; such decay was validated by numerical studies in [22].

The above discussion underscores that the time-reversal image quality degrades with decorrelation of the actual Green's function and that used when performing time-reversal imaging. This suggests that imaging quality may be maintained even if the exact media (Green's function) are unknown, as long as there is a sufficient correlation between the actual and simulated media. In the work that follows, we assume that the actual Green's function is unknown and that it represents one sample from an underlying random process (the random process captures our understanding of the range of Green's functions from which the actual Green's function is sampled). Moreover, while the true Green's function is unknown, we assume access to an ensemble of Green's functions sampled from the aforementioned random process. The above review suggests that, if the ensemble of Green's functions (or the associated subspace) is sufficiently correlated to the true Green's function, it should be possible to obtain useful imaging quality.

III. IMAGING IN CHANGING ENVIRONMENTS

In this section, we examine ETR imaging in changing environments. In particular, we make the assumption that the precise Green's function used in the forward process (associated with the measured scattered fields) is unknown; however, we assume access to an ensemble of K Green's functions $\{G_k(\omega, \mathbf{r}_n, \mathbf{r})\}_{k=1,K}$. We first review the basic time-reversal imaging technique, followed by a discussion of how the ensemble of Green's functions $\{G_k(\omega, \mathbf{r}_n, \mathbf{r})\}_{k=1,K}$ may be employed.

A. Time-Reversal Imaging

We consider a 2-D problem, with a localized (small relative to wavelength) target situated at \mathbf{r}_t . We assume that the source is located at \mathbf{r}_{n_0} , and the n th receiving antenna at \mathbf{r}_n , and a set of N receiver antennas are employed. The scattered field measured by the n th antenna due to this target is $S(\omega, \mathbf{r}_n, \mathbf{r}_{n_0})$.

An ETR space-time image is computed using Green's function k as [5]

$$I_k(t, \mathbf{r} | \mathbf{r}_{n_0}) = \left| \sum_{n=1}^N \int_{\omega_{BW}} d\omega S^*(\omega, \mathbf{r}_n, \mathbf{r}_{n_0}) G_k(\omega, \mathbf{r}, \mathbf{r}_n) \times G_k(\omega, \mathbf{r}_{n_0}, \mathbf{r}) \exp(-j\omega t) \right| \quad (1)$$

where the Fourier integral is performed over the system bandwidth ω_{BW} and $*$ denotes complex conjugate.

Assume that the Green's function characteristic of the scattered fields is represented as $G_0(\omega, \mathbf{r}_n, \mathbf{r})$; the corresponding scattered field $S(\omega, \mathbf{r}_n, \mathbf{r}_{n_0})$ can be expressed as $S(\omega, \mathbf{r}_n, \mathbf{r}_{n_0}) = B(\omega) G_0(\omega, \mathbf{r}_n, \mathbf{r}_t) G_0(\omega, \mathbf{r}_t, \mathbf{r}_{n_0})$, with the antenna response embedded in the Green's functions and $B(\omega)$ representing the spectrum of the excitation. Refocusing at $\mathbf{r} = \mathbf{r}_t$ is expected at time $t = 0$ for the case in which $G_k(\omega, \mathbf{r}_n, \mathbf{r})$ matches $G_0(\omega, \mathbf{r}_n, \mathbf{r})$ [8], although we assume here that all members of the ensemble $\{G_k(\omega, \mathbf{r}_n, \mathbf{r})\}_{k=1,K}$ are distinct from $G_0(\omega, \mathbf{r}_n, \mathbf{r})$.

Typically, the scattering data and Green's function are sampled at discrete frequencies, and the image at $t = 0$ is expressed as

$$I_k(t = 0, \mathbf{r} | \mathbf{r}_{n_0}) = \left| \sum_{n=1}^N \mathbf{s}^H(n, n_0) \mathbf{g}_k(n_0, \mathbf{r}, n) \right| \quad (2)$$

where $\mathbf{s}(n, n_0)$ is an $N_f \times 1$ vector representing the frequency dependence of $S(\omega, \mathbf{r}_n, \mathbf{r}_{n_0})$ at N_f chosen frequencies, $\mathbf{g}_k(n_0, \mathbf{r}, n)$ is an $N_f \times 1$ vector representing the frequency dependence of the product $g_k(\omega, \mathbf{r}_{n_0}, \mathbf{r}, \mathbf{r}_n) = G_k(\omega, \mathbf{r}, \mathbf{r}_n) G_k(\omega, \mathbf{r}_{n_0}, \mathbf{r})$ at those N_f frequencies, and the superscript H represents complex transpose. If each antenna sequentially plays the role of the source, with scattering data measured at all N antennas, we obtain a time-reversal image by averaging across excitations

$$I_k(t = 0, \mathbf{r}) = \frac{1}{N} \left| \sum_{n_0=1}^N \sum_{n=1}^N \mathbf{s}^H(n, n_0) \mathbf{g}_k(n_0, \mathbf{r}, n) \right|. \quad (3)$$

In the above discussion, we have used one of the mismatched members of the ensemble $\{G_k(\omega, \mathbf{r}_n, \mathbf{r})\}_{k=1,K}$ to yield a corresponding time-reversal image. There has been a theoretical and experimental research [8], [20]–[22] that demonstrates that the time-reversal quality may deteriorate precipitously as the degree of mismatch between $G_k(\omega, \mathbf{r}_n, \mathbf{r})$ and $G_0(\omega, \mathbf{r}_n, \mathbf{r})$ increases—as discussed in Section II, as the media underlying $G_k(\omega, \mathbf{r}_n, \mathbf{r})$ and $G_0(\omega, \mathbf{r}_n, \mathbf{r})$ become increasingly decorrelated.

Since we assume access to the entire ensemble $\{G_k(\omega, \mathbf{r}_n, \mathbf{r})\}_{k=1,K}$ rather than producing an image based on a single Green's function, one may consider using all of the information in $\{G_k(\omega, \mathbf{r}_n, \mathbf{r})\}_{k=1,K}$ through a simultaneous use of all K Green's functions. Below, we consider several alternatives for this strategy, with the performance on the measured data considered in Section V.

B. Time-Reversal Imaging With Average and PCA Green's Function

The simplest approach one might consider would be simply to use the average Green's function

$$\mathbf{g}_{\text{avg}}(n_0, \mathbf{r}, n) = \frac{1}{K} \sum_{k=1}^K \mathbf{g}_k(n_0, \mathbf{r}, n) \quad (4)$$

yielding a time-reversal image

$$I_{\text{avg}}(t=0, \mathbf{r}) = \frac{1}{N} \left| \sum_{n_0=1}^N \sum_{n=1}^N \mathbf{s}^H(n, n_0) \mathbf{g}_{\text{avg}}(n_0, \mathbf{r}, n) \right| \quad (5)$$

where $\mathbf{g}_{\text{avg}}(n_0, \mathbf{r}, n)$ is an $N_f \times 1$ column vector representing the frequency dependence of the average Green's function.

A similar use of the ensemble of Green's functions is considered via an eigen analysis, analogous to PCA [19]. We perform an eigen decomposition of the $N_f \times N_f$ matrix

$$\mathbf{G}(n_0, \mathbf{r}, n) = \sum_{k=1}^K \mathbf{g}_k(n_0, \mathbf{r}, n) \mathbf{g}_k(n_0, \mathbf{r}, n)^H. \quad (6)$$

Let $\mathbf{w}_l(n_0, \mathbf{r}, n)$ represents the l th eigenvector of (6) corresponding to the l th largest eigenvalue; note that the eigen analysis is performed at all potential imaging points \mathbf{r} . Considering that the dominant eigenvectors have arbitrary phasing, we incoherently sum over elements. A PCA-based imaging result is represented as

$$I_{\text{PCA}}(t=0, \mathbf{r}) = \frac{1}{N} \sum_{n_0=1}^N \sum_{n=1}^N \left| \sum_{l=1}^{L_P} \mathbf{s}^H(n_0, n) \mathbf{w}_l(n_0, \mathbf{r}, n) \right|. \quad (7)$$

In the example results (see Section V), we consider $L_P = 1$ principal component.

C. Wideband MV-EPC

To enhance the imaging quality and robustness, we developed a wideband MV-EPC algorithm, this representing an extension of a related technique applied previously to problems involving narrowband signals and large array apertures [10]. The wideband MV-EPC beamformer weight \mathbf{w}_F is estimated by minimizing the beamformer output power $Z_F = \mathbf{w}_F^H \mathbf{R}_F \mathbf{w}_F$, subject to the frequency perturbation constraints $\mathbf{G}_F^H \mathbf{w}_F = \mathbf{G}_F^H \mathbf{h}_{F1}$, from which we can deduce the equivalent constraint $\mathbf{H}_F^H \mathbf{w}_F = \mathbf{e}_1$. The matrix \mathbf{R}_F is of dimension $N_f \times N_f$ and is computed as

$$\mathbf{R}_F = \frac{1}{N^2} \sum_{n_0=1}^N \sum_{n=1}^N \mathbf{s}(n, n_0) \mathbf{s}^H(n, n_0) \quad (8)$$

where $\mathbf{s}(n, n_0)$ is an $N_f \times 1$ column vector representing the frequency dependence of $S(\omega, \mathbf{r}_n, \mathbf{r}_{n_0})$. Note that $\mathbf{s}(n, n_0)$ is identical with the expression in (2) employed within the time-reversal imager. We are employing the frequency dependence to effect high-quality images and assume that the N antennas are proximate to one another relative to the dominant wavelength

(details are discussed further in Section V, for the particular data considered here).

The constraint matrix \mathbf{G}_F , for antennas at \mathbf{r}_n and \mathbf{r}_{n_0} , represents K different media realizations and is represented as

$$\mathbf{G}_F(n, \mathbf{r}, n_0) = [\mathbf{g}_1, \dots, \mathbf{g}_K] \quad (9)$$

where $\mathbf{g}_k(n, \mathbf{r}, n_0)$ is an $N_f \times 1$ vector representing the frequency dependence of product $g_k(\omega, \mathbf{r}_{n_0}, \mathbf{r}, \mathbf{r}_n) = G_k(\omega, \mathbf{r}, \mathbf{r}_n) G_k(\omega, \mathbf{r}_{n_0}, \mathbf{r})$. We perform a singular value decomposition (SVD) on the $N_f \times K$ constraint matrix \mathbf{G}_F to obtain the dominant constraint space of rank D_F

$$\mathbf{G}_F(n, \mathbf{r}, n_0) = \mathbf{H}_F \mathbf{\Lambda}_F \mathbf{\Gamma}_F^H \quad (10)$$

where \mathbf{H}_F is a $N_f \times D_F$ matrix whose columns are the left singular vectors of \mathbf{G}_F , $\mathbf{\Lambda}_F$ is a $D_F \times D_F$ diagonal matrix of the singular values of \mathbf{G}_F , and $\mathbf{\Gamma}_F$ is a $K \times D_F$ matrix whose columns are the right singular vectors of \mathbf{G}_F . In the example results, we consider $D_F = K$.

The left dominant singular vectors can be demonstrated theoretically to be equivalent to the PCA vectors. A PCA-based adaptive time-reversal imaging can be performed using the left singular vector corresponding to the largest singular value of \mathbf{G}_F [14]

$$\mathbf{w}_{\text{PCA}}(n, \mathbf{r}, n_0) = \mathbf{H}_F \mathbf{e}_1. \quad (11)$$

The wideband MV-EPC weight is given by

$$\mathbf{w}_F(n, \mathbf{r}, n_0) = \mathbf{R}_F^{-1} \mathbf{H}_F (\mathbf{H}_F^H \mathbf{R}_F^{-1} \mathbf{H}_F)^{-1} \mathbf{e}_1 \quad (12)$$

and a wideband MV-EPC-based time-reversal image is represented as

$$I_{\text{FPC}}(t=0, \mathbf{r}) = \sum_{n_0=1}^N \sum_{n=1}^N |\mathbf{s}^H(n, n_0) \mathbf{w}_F(n, \mathbf{r}, n_0)|. \quad (13)$$

From expressions (8)–(13), we observe that wideband MV-EPC maintains the frequency dependence of the Green's function throughout the algorithm, which benefits time-reversal imaging [in (13) we perform coherent processing across the frequency and incoherent processing across the source and observation point].

IV. EXPERIMENTAL CONFIGURATION

A. Measurement Setup

The ideas outlined in Sections II and III are examined based upon controlled electromagnetic scattering measurements. In these experiments, we extend many previous measurements performed with acoustic and ultrasonic systems [2], [3], as well as recent electromagnetic studies [1], [5], [8]. As discussed in Section I, time reversal is most appropriate in the media characterized by a high level of scattering and multipath. We have therefore constituted a highly scattering random medium by employing 680 low-loss dielectric rods (plexiglass), as shown in Fig. 2. The rods are 1.25 cm in diameter and 0.6 m in length, and its approximate dielectric constant $\varepsilon_r = 2.5$; the rods were

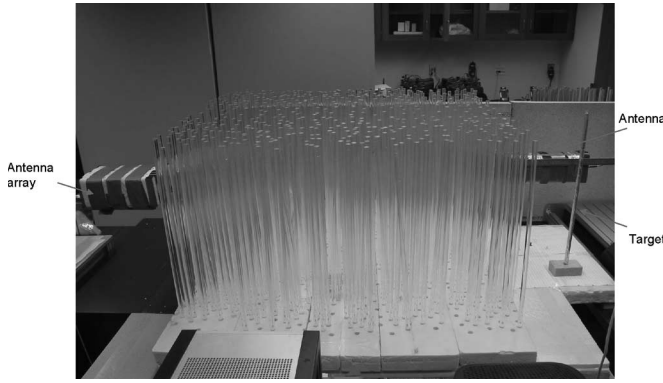


Fig. 2. Dielectric rod setup used in the experimental time-reversal studies. The right antenna is moved using a precision stepper motor, in the absence of the target, to measure the Green's function. The size of the dielectric rod domain is 1.0 m \times 1.2 m.

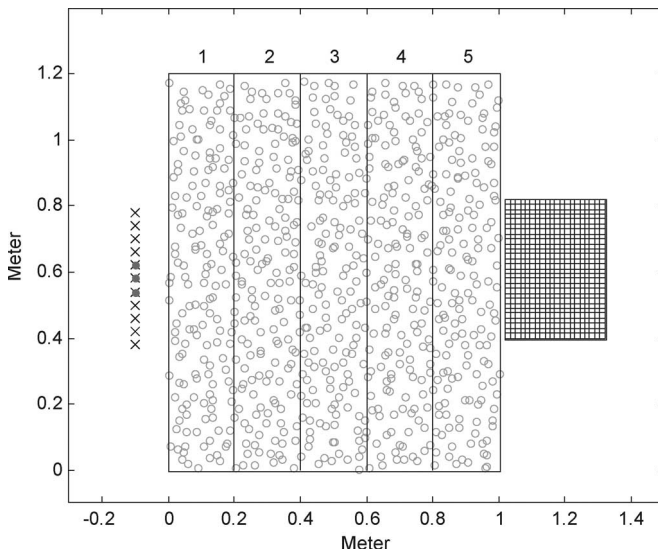


Fig. 3. Top schematic view of the rods in Fig. 2. The rods are decomposed into five regions, with the rods in each region held together at the bottom via styrofoam. Different media instantiations are implemented by interchanging the positions of the five rod regions. The marks "x" to the left-hand side show the antenna positions of SAR imaging. Three "x" covered by dots represent the physical array used for the time-reversal imaging. The right grid domain is the imaging domain of size 30 cm \times 42 cm, with each grid point scanned by an antenna.

distributed in a random manner (with no particular distribution, although the average interrod spacing was 4.5 cm between rod axes). The rods are situated in a domain 1.0 m long and 1.2 m wide, embedded at the bottom in styrofoam ($\epsilon_r \approx 1$). The 1.0 \times 1.2 m² rod domain is composed of five distinct and contiguous rod sections (see Fig. 3); each is 20 cm long and 1.2 m wide (there are five distinct styrofoam sections). Different realizations of the environment are manifested by interchanging the relative position of these five sections of rods. A target is constituted by wrapping a rod with aluminum foil, with these targets placed to the right of the random medium (see Figs. 2 and 3).

An N -element linear sensor array ($N = 3$ in our case) is placed to the left of the random media (see Fig. 3), with the interelement spacing $\Delta = 4.0$ cm. The antennas are placed at a height that bisects the midpoint of the rods, and the measurements are approximately 2-D. The elements of the array are identical Vivaldi antennas over the 0.5–10.5-GHz

band, with the electric fields vertically polarized (electric fields parallel to the rod axes). The measurements are performed with a vector network analyzer.

The three antennas to the left of the medium are fixed. We require a means of obtaining the ensemble of Green's functions $\{G_k(\omega, \mathbf{r}_n, \mathbf{r})\}_{k=1,K}$, where \mathbf{r} corresponds to an imaging position to the right of the domain of interest (in which the target may exist; see Fig. 3). To obtain these Green's functions, a receiving antenna is placed on a stepper motor, at position \mathbf{r} , and it is used to sequentially measure the transmitted fields from the n th antenna at the left, located at \mathbf{r}_n . The stepper motor is deployed at a sampling rate of $\Delta_x = \Delta_y = 1.5$ cm in two dimensions (over a domain of size 30 cm \times 42 cm, and it is within this domain that targets are placed and imaging considered). The K different media realizations are manifested by changing the relative positions of the five rod regions (see Fig. 3), and in the examples that follow, all five regions are placed differently relative to the actual media for which the scattering measurements are performed (i.e., the ensemble of Green's functions $\{G_k(\omega, \mathbf{r}_n, \mathbf{r})\}_{k=1,K}$ is a characteristic of K different media realizations, as implemented in Fig. 3, and each of the five media regions is distinct from the media corresponding to $G_0(\omega, \mathbf{r}_n, \mathbf{r})$ and the forward measurements).

It is desirable to compare the algorithms discussed in Section III to more traditional approaches. SAR is a common technique for imaging a target in a complex scattering environment. In SAR, we do not require the ensemble of Green's functions $\{G_k(\omega, \mathbf{r}_n, \mathbf{r})\}_{k=1,K}$, since typically, one simply employs the free-space Green's function. However, in SAR, one obtains imaging resolution by utilizing a large (synthetic) aperture. For comparison to SAR, we also consider measurements in which a single antenna is employed at left (see Fig. 3) to perform the scattering measurements, with this antenna placed on a stepper motor. The stepper motor is displaced along a linear path with a sampling rate of 4 cm.

B. Change Detection

The media considered in these experiments is highly scattering, yielding a very strong clutter signature, in addition to the relatively weak scattering from the target (when present). If one attempts target imaging based on the scattered fields alone, very poor results are obtained because the scattered fields are dominated by the clutter (rather than the target). Therefore, in the results that follow, all imaging is performed based on the signal manifested by change detection. Specifically, it is assumed that scattering data are obtained in the absence of any targets (i.e., a background-scattered signal). A second measurement is then performed with the same rod medium, but now with the addition of a target. The data with which imaging is performed are based on the difference between these two signals. This is termed change detection [5], and it is widely employed in SAR processing in highly scattering environments.

V. EXAMPLE IMAGING RESULTS AND ANALYSIS

In the results that follow, the target was composed of a single rod of the type used to constitute the highly scattering

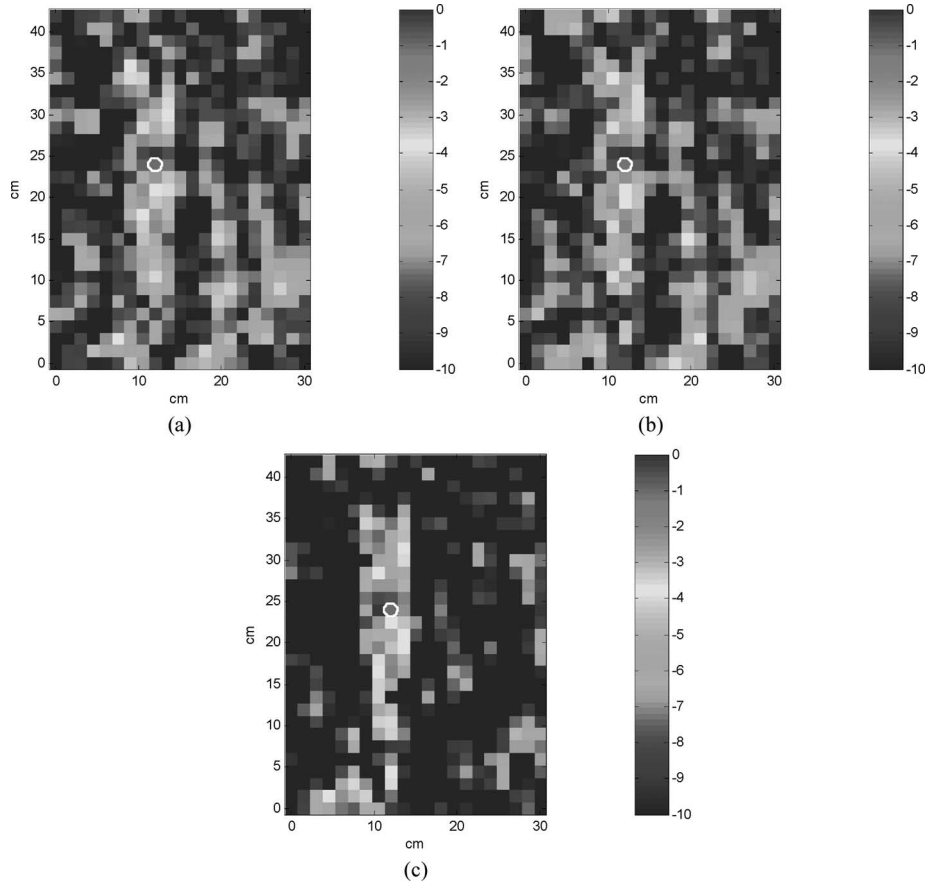


Fig. 4. Representative imaging results using full-band scattering data, with Green's functions estimated by (a) the average, (b) PCA, and (c) MV-EPC techniques.

media; the rod was wrapped with aluminum foil to constitute a relatively strong scatterer (although, in the absence of change detection, the signature of the target is buried in the clutter induced by the 680 dielectric rods). The target was situated in the imaging region (see Fig. 3) over which the Green's functions were measured (although not at a specific—discrete—point at which the Green's function was measured). The target was placed in 24 distinct places within the imaging region to constitute different realizations of the scattering data, for statistical characterization of the imaging and detection algorithms.

The Green's functions within the imaging domain were measured separately for 15 distinct arrangements of the five dielectric-rod regions (see Fig. 3); across the 15 different media realizations, there was no overlap in the placement of any of the five dielectric regions, i.e., there was a complete mismatch in the rod locations when comparing any one of the 15 realizations to another. In addition, for each of the 15 distinct media arrangements, we measured separate target-scattering data for the aforementioned 24 different target positions. We note that, while there is no overlap in the positions of the five rod regions between the 15 different media realizations, it cannot be claimed that the measurements are independent, since clearly, the underlying five constitutive regions remain unchanged.

Although the particular media characteristic of the scattering data is assumed unknown, several of the imaging techniques discussed in Section III employ an ensemble of Green's func-

tions, with this implemented as follows. Assume that scattering data were collected for media associated with one of the 15 media realizations; when imaging, we consider $K = 14$, with $\{G_k(\omega, \mathbf{r}_n, \mathbf{r})\}_{k=1, K}$ composed of the remaining set of Green's functions (from the distinct media arrangements).

As indicated above, the measurements were performed in the frequency domain over the 0.5–10.5-GHz bandwidth. We consider imaging results when all frequency-domain data are used, as well as results based on a carefully selected (discussed below) subband of frequencies. In addition to presenting a set of qualitative results in the form of images, we present quantitative results, in the form of the receiver operating characteristic (ROC).

A. Imagery Based on Full-Band Data

We first perform imaging based on the full-band data measured from 0.5–10.5 GHz, with 201 uniform frequency samples. All imaging results are plotted with a 10-dB dynamic range, represented with a color bar, and the peak value in each image is normalized to 0 dB. The target position is indicated by the white circle in each image. Fig. 4(a)–(c) presents typical results for $I_{\text{avg}}(t = 0, \mathbf{r})$, $I_{\text{PCA}}(t = 0, \mathbf{r})$, and $I_{\text{FPC}}(t = 0, \mathbf{r})$, respectively, for which good imaging quality is observed. We observe that the wideband MV-EPC suppresses more sidelobes than the averaging and PCA techniques, yielding the best result among the three techniques.

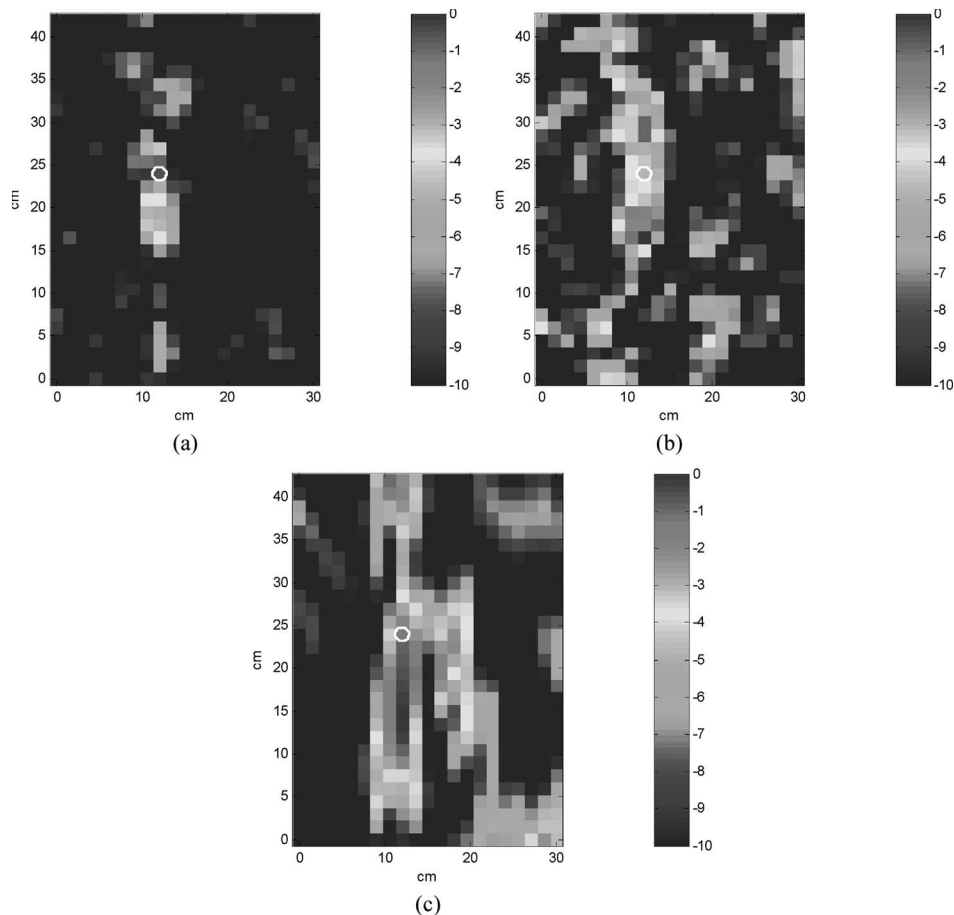


Fig. 5. Representative imaging using (a) a time-reversal mirror (TRM) with a matched Green's function, (b) TRM with a single mismatched Green's function, and (c) SAR imaging.

By using the full-band data (0.5–10.5 GHz), the measured cross-range resolution in Fig. 4 is approximately 6 cm, with approximately 3 cm down-range. For a homogeneous medium, the anticipated cross-range resolution is $R_c = \lambda L/a$, where λ is the wavelength, a is the real linear aperture length, and L is the distance from the aperture center to the imaging point. If we consider a free-space medium, the center frequency is 5.5 GHz, a real aperture $a = 8$ cm, and length $L = 1.2$ m, the optimal free-space cross-range resolution is $R_c = 81.8$ cm; the 6-cm time-reversal resolution, relative to $R_c = 81.8$ cm, demonstrates the significant improvement in cross-range resolution manifested by the rod-induced multipath. Regarding computation time, it requires roughly 3.5 min of CPU time in Matlab on a Pentium IV personal computer with a 1.73-GHz CPU for the wideband MV-EPC algorithm to synthesize a 21×29 pixel image, versus 7 s for the averaging method and 12 s for the PCA technique.

As a reference, in Fig. 5, we show representative imaging results for time-reversal imaging using a single Green's function in the imaging phase. In Fig. 5(a), the Green's function used in time-reversal method corresponds to the actual media considered in the scattering data, while in Fig. 5(b), one of the 14 mismatched Green's functions is utilized when performing time reversal. In Fig. 5(a), a very tight focus is observed at the target, while in Fig. 5(b), there are more sidelobes [we again underscore the tight cross-range resolution of the time-reversal

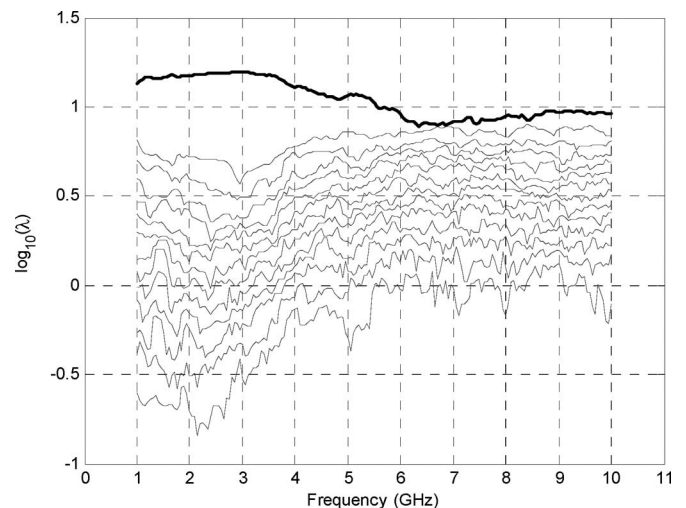


Fig. 6. Logarithm of the 14 singular values of the windowed constraint matrix as a function of the center frequency of the sliding window, which is of the width 1 GHz (21 frequency samples). The black curve represents the spectrum of the largest singular value.

image, particularly for the matched case in Fig. 5(a), relative to $R_c = 81.8$ cm for the same aperture size in free space]. When considering multiple results of the form in Fig. 5(b)—time reversal with mismatched Green's function—we observed the predicted [4] instability in the image quality and in focusing at

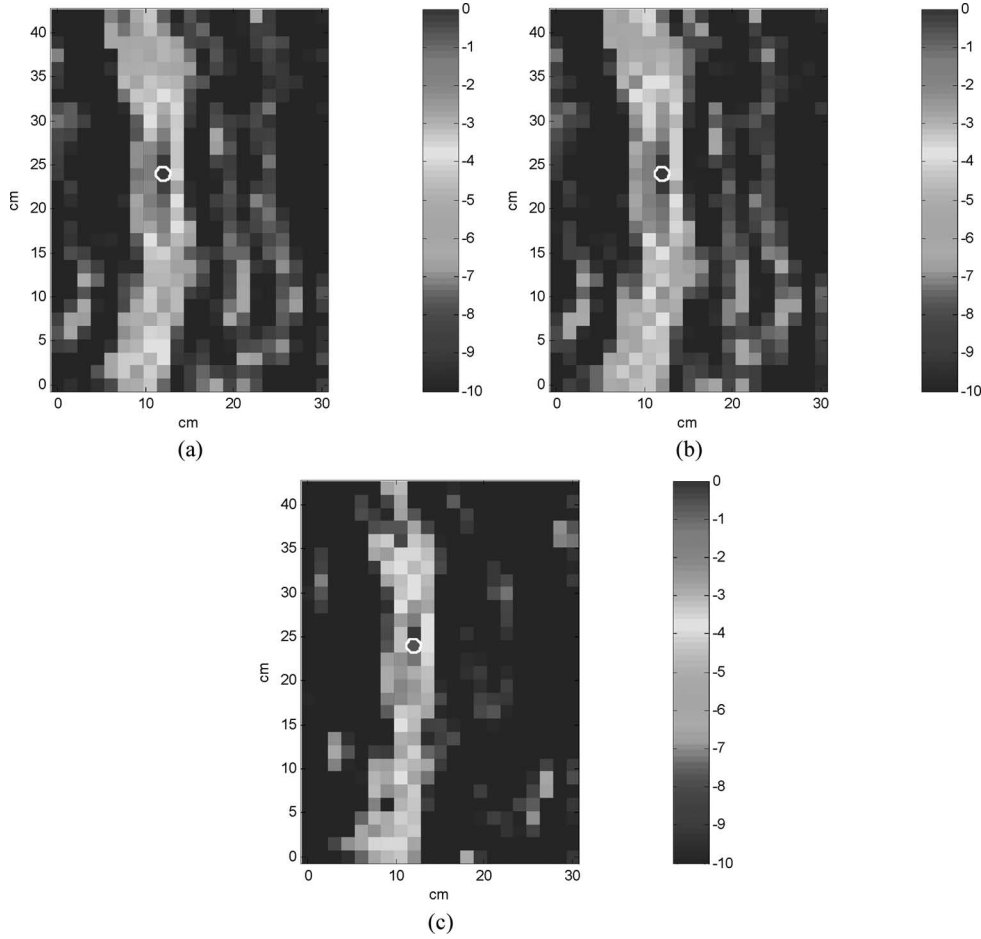


Fig. 7. Time reversal with the 1–6-GHz subband, with the Green's functions addressed via (a) averaging, (b) PCA, and (c) MV-EPC.

the proper target location. In Fig. 5(c), we present SAR imaging results, for which the free-space Green's function is applied, and the linear aperture (with target in the center of the aperture) is 40 cm, with a 4-cm sampling. Poor SAR imaging performance is observed, even with the large aperture size (five times the size of the aperture used in the other imaging techniques), with this manifested by the highly scattering environment and hence mismatch to the free-space Green's function.

The results in Figs. 4 and 5 represent our experience with the techniques considered here. Specifically, direct time reversal with a mismatched Green's function yields unstable results, meaning that the performance is dependent on the particular scattering data and the particular mismatched Green's function considered. This is consistent with the theoretical predictions. We note that this variability or instability in the time-reversal imaging quality with the mismatched Green's function is indicative of a decorrelation between the media used in the forward scattering measurement and the inverse time-reversal imaging. However, the results in Fig. 4 indicate that, by utilizing knowledge of the subspace in which the Green's function lives, defined by the ensemble $\{G_k(\omega, \mathbf{r}_n, \mathbf{r})\}_{k=1,K}$, it is possible to recover imaging quality despite the fact that the specific Green's function is unknown. These qualitative observations in imaging quality will be made quantitative below in Section V-C.

B. Example Results of Subband Imaging

The results discussed above were based on the utilization of the full-scattering bandwidth. However, the quality of the imaging results is anticipated to be linked to the correlation between the Green's function used in the forward measurement and in the inverse imaging phase. The sensitivity of the Green's function on the specific media realization is connected to the media variation relative to the wavelength. Therefore, one would anticipate that the imaging quality and sensitivity to Green's function uncertainty will be dictated by the frequencies considered in the measurements. We address this question in the following analysis.

Recall that we have measured frequency-dependent Green's functions $\mathbf{G}_F(n, \mathbf{r}, n_0) = [\mathbf{g}_1, \dots, \mathbf{g}_K]$, where $g_k(\omega, \mathbf{r}_{n_0}, \mathbf{r}, \mathbf{r}_n) = G_k(\omega, \mathbf{r}, \mathbf{r}_n)G_k(\omega, \mathbf{r}_{n_0}, \mathbf{r})$ accounts for the two-way propagation from a source antenna at \mathbf{r}_{n_0} to point \mathbf{r} in the imaging domain and from \mathbf{r} to the receiver antenna at \mathbf{r}_n . To explore the singular-value spectrum across the frequency, we apply a sliding window of width 1 GHz (21 frequency samples) on the constraint matrix \mathbf{G}_F , and in Fig. 6, we show the singular-value spectrum for $K = 14$ distinct media as a function of the center frequency of the sliding window. We note that there is a single dominant singular value in the frequency subband of 1–6 GHz, implying that, in this frequency range, the different media are highly correlated (wavelength is relatively

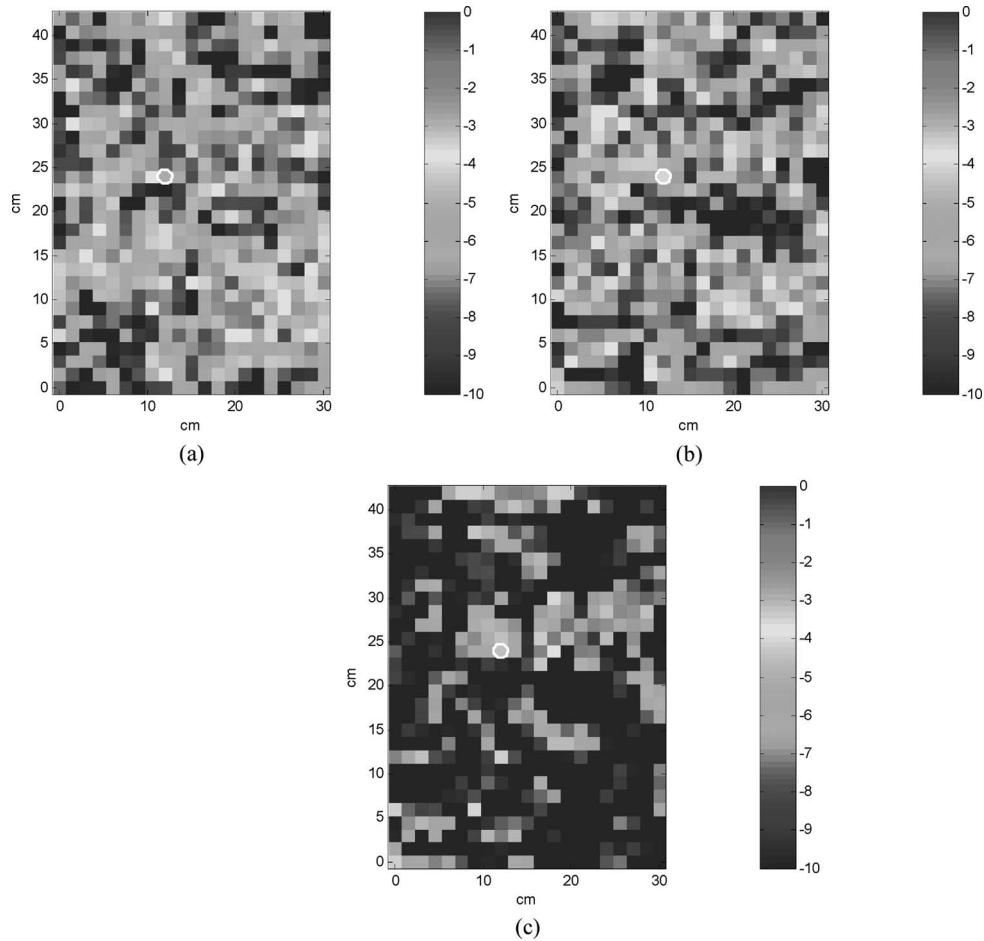


Fig. 8. Imaging with the 5–10-GHz subband, with the Green's functions addressed via (a) averaging, (b) PCA, and (c) MV-EPC.

large with respect to the interrod spacing and therefore less sensitivity to media variation). Above 6 GHz, there is no longer a clear dominant singular value, suggesting a greater degree of wave mixing in the highly scattering media and therefore anticipating greater requirements for knowledge of the true Green's function when performing imaging.

We consider the performance of the average, PCA, and MV-EPC algorithms in the two frequency-dependent domains indicated above: 1) from 1–6 GHz and 2) from 5–10 GHz, with results for these cases shown in Figs. 7 and 8, respectively. The results in Fig. 7 are of relatively high quality (good focusing about the target location), while the 5–10-GHz band alone (Fig. 8) yields poor results. It is of interest to compare the results in Fig. 7 to the full-band results in Fig. 4, for which the same imaging techniques were applied. While the high-frequency data alone yield relatively poor imaging performance (Fig. 8), we note, when comparing Figs. 4 and 7, that the high frequencies, when combined with the 1–6-GHz band, improve the tightness of the focus around the target. The quantitative analysis that follows is based on the full-band scattering data.

C. Quantitative Analysis of Imaging Results

As indicated above, a large number of images with different imaging techniques have been generated by varying the placement of the target (24 target locations); space limitations

prohibit showing all imagery, with the results presented above being representative. It is therefore of interest to perform a quantitative analysis of all such images, where here, this is quantified in terms of the detection performance. To achieve this, a square box is defined corresponding to a contiguous 5×5 pixel (or $7.5 \text{ cm} \times 7.5 \text{ cm}$) window in image space, and the test statistic l is the peak amplitude within this box. Recall that the images presented above were composed of a total of 21×29 pixels. If a portion of the box encompasses the target, then the target is assumed present, and if not, there is no target. A false alarm is defined when a target is declared within a region for which the target is not located, while a target is missed if a target is not declared when it is in fact located within the 5×5 pixel region. Based on this definition, the ROC of images is investigated. Specifically, to compute the ROC, we set a threshold T , and if $l \geq T$, a target is declared. By varying the threshold T from zero to l_{\max} (the largest value of l within a given image), an ROC is obtained, which represents the probability of detection as a function of the probability of false alarm. We note that l_{\max} does not necessarily correspond to the position of the target, so having T always less than l_{\max} does not imply we always have a probability of detection of one.

In Fig. 9, we plot the ROC curves for all techniques considered here. We note that the wideband MV-EPC (13) yields the best performance, and the performance of the average and

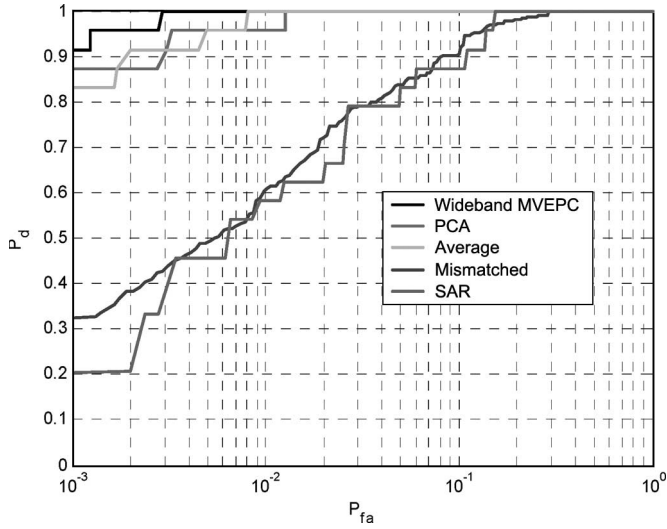


Fig. 9. ROC curves for the different imaging techniques based on the full-band imaging results.

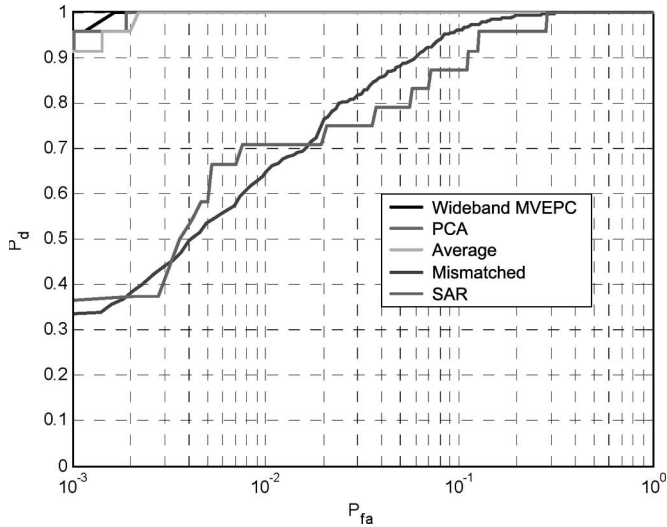


Fig. 10. ROC curves for different imaging techniques based on the 1–6-GHz subband imaging results.

the PCA techniques [(5) and (7), respectively] are comparable. These results are averaged across all 15 different media and across all 24 target locations. For the case of time reversal with mismatched Green's function, the results are averaged across all possible combinations of mismatched Green's functions.

The results in Fig. 9 considered full-band data, and in Fig. 10, we present results for the 1–6-GHz subband, over which there was a dominant singular value (see Fig. 6). We note that the ROC performance of the various algorithms is improved when using the subband over which there is a dominant singular value. This indicates that, while the focusing quality of the full-band data is superior to that of the subband data (comparing Figs. 4 and 7), the subband data are less beset by spurious sidelobes, which undermine the ROC performance. This suggests that detection may best be performed by using the lower-frequency bands, over which there is a dominant singular value, with classification (for which resolution is important) based on the full-band data.

VI. CONCLUSION

Time-reversal imaging has been examined experimentally for electromagnetic target detection in the highly scattering uncertain media. We addressed time-reversal behavior for the case in which the media employed in the forward and inverse steps are mismatched.

We consider techniques for the case in which the media employed are uncertain, represented by an ensemble of the Green's functions. Besides straightforward methods such as averaging and PCA, we extend a wideband MV-EPC, in which the unknown Green's function is constrained to reside in a subspace spanned by the Green's function ensemble. The imaging results show that the wideband MV-EPC suppresses more sidelobes than the average and PCA techniques, yielding the best result among the three techniques.

It has been demonstrated that access to an ensemble of Green's functions $\{G_k(\omega, \mathbf{r}_n, \mathbf{r})\}_{k=1,K}$ can improve time-reversal imaging quality, in the absence of the true Green's function, assuming we are operating in a regime (frequencies) for which there is still a dominant propagation mechanism; this implies that the ensemble of Green's functions $\{G_k(\omega, \mathbf{r}_n, \mathbf{r})\}_{k=1,K}$ reside within a low-dimensional subspace (see Fig. 6). There is still the practical problem of how this may be achieved in a realistic sensing scenario, i.e., how one might practically measure the ensemble $\{G_k(\omega, \mathbf{r}_n, \mathbf{r})\}_{k=1,K}$. We provide one example here. Assume there is interest in imaging vehicles on roads, but the roads are buried under a foliage canopy, and it is undesirable to use an array of cameras (e.g., there is a desire for covert surveillance). A distant transmitting antenna(s) may be employed, and vehicles with antennas may be utilized to measure the Green's function from the source antenna(s) to the road(s) of interest. These Green's function measurements may be performed periodically (daily, weekly, monthly, etc.) to constitute an ensemble, accounting for variation in the propagation (foliage) properties. The ensemble of measured Green's functions may then be used in the manner considered here, to perform covert nonline-of-site imaging of the roads. The same idea may be employed within the "canyons" of major cities.

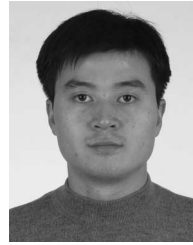
We close by noting the following, which was brought to our attention by one of the anonymous reviewers. The weights \mathbf{w}_F in our wideband MV-EPC algorithm depend on the matrix of the left singular vectors \mathbf{H}_F of the constraint matrix \mathbf{G}_F . One could also calculate them from the product $\mathbf{G}_F \mathbf{G}_F^H = \mathbf{H}_F \mathbf{\Lambda} \mathbf{\Lambda}^H \mathbf{H}_F^H$, which is an ensemble average over the Green's function realizations. Since this depends only on the statistics of the Green's function, it might be possible to obtain acceptable weighting vectors using a statistical model. The authors thank the reviewer for this very insightful observation and feel it is a worthy direction of further research.

REFERENCES

- [1] G. Lerosey, J. de Rosny, A. Tourin, A. Derode, G. Montaldo, and M. Fink, "Time reversal of electromagnetic waves," *Phys. Rev. Lett.*, vol. 92, no. 19, May 2004.
- [2] J. de Rosny, A. Tourin, A. Derode, B. van Tiggelen, and M. Fink, "The relation between time reversal focusing and coherent backscattering in multiple scattering media: A diagrammatic approach," *Phys. Rev. E, Stat.*

Phys. Plasmas Fluids Relat. Interdiscip. Top., vol. 70, no. 4, p. 046 601, Oct. 2004.

- [3] M. Fink, "Time reversed acoustics," *Phys. Today*, vol. 50, no. 3, pp. 34–40, Mar. 1997.
- [4] P. Blomberg, G. Papanicolaou, and H. K. Zhao, "Super-resolution in time-reversal acoustics," *J. Acoust. Soc. Amer.*, vol. 111, no. 1, pp. 230–248, Jan. 2002.
- [5] D. Liu, G. Kang, L. Li, Y. Chen, S. Vasudevan, W. Joines, Q. H. Liu, J. Krolik, and L. Carin, "Electromagnetic time-reversal imaging of a target in a cluttered environment," *IEEE Trans. Antennas Propag.*, vol. 53, no. 9, pp. 3058–3066, Sep. 2005.
- [6] D. Dowling and D. Jackson, "Narrow-band performance of phase-conjugate arrays in dynamic random media," *J. Acoust. Soc. Amer.*, vol. 91, no. 6, pp. 3257–3277, Jun. 1992.
- [7] A. Derode, P. Roux, and M. Fink, "Robust acoustic time reversal with high-order multiple scattering," *Phys. Rev. Lett.*, vol. 75, no. 23, pp. 4206–4209, Dec. 1995.
- [8] D. Liu, S. Vasudevan, J. Krolik, G. Bal, and L. Carin, "Electromagnetic time-reversal source localization in changing media: Experiment and analysis," *IEEE Trans. Antennas Propag.*, vol. 55, no. 2, pp. 344–354, Feb. 2007.
- [9] H. Schmidt, A. B. Baggeroer, W. A. Kuperman, and E. K. Scheer, "Environmentally tolerant beamforming for high-resolution matched field processing: Deterministic mismatch," *J. Acoust. Soc. Amer.*, vol. 88, no. 4, pp. 1851–1862, Oct. 1990.
- [10] J. L. Krolik, "Matched-field minimum variance beamforming in a random ocean channel," *J. Acoust. Soc. Amer.*, vol. 92, no. 3, pp. 1408–1419, Sep. 1992.
- [11] A. Tourin, A. Derode, and M. Fink, "Sensitivity to perturbations of a time-reversed acoustic wave in a multiple scattering medium," *Phys. Rev. Lett.*, vol. 87, no. 27, pp. 24301–1–24301–4, Dec. 2001.
- [12] J. L. Krolik, "The performance of matched-field beamformers with Mediterranean vertical array data," *IEEE Trans. Signal Process.*, vol. 44, no. 10, pp. 2605–2611, Oct. 1996.
- [13] S. P. Czenszak and J. L. Krolik, "Robust wideband matched-field processing with a short vertical array," *J. Acoust. Soc. Amer.*, vol. 101, no. 2, pp. 749–759, Feb. 1997.
- [14] S. Kim, W. A. Kuperman, W. S. Hodgkiss, H. C. Song, G. F. Edelmann, and T. Akal, "Robust time reversal focusing in the ocean," *J. Acoust. Soc. Amer.*, vol. 114, no. 1, pp. 145–157, Jul. 2003.
- [15] G. J. Orris, J. Nicholas, and J. S. Perkins, "The matched-phase coherent multi-frequency matched-field process," *J. Acoust. Soc. Am.*, vol. 107, no. 5, pp. 2563–2575, 2000.
- [16] W. A. Kuperman, W. S. Hodgkiss, H. C. Song, T. Akal, C. Ferla, and D. R. Jackson, "Phase conjugation in the ocean: Experimental demonstration of an acoustic time-reversal mirror," *J. Acoust. Soc. Amer.*, vol. 103, no. 1, pp. 25–40, Jan. 1998.
- [17] H. C. Song, W. A. Kuperman, W. S. Hodgkiss, T. Akal, and C. Ferla, "Iterative time reversal in the ocean," *J. Acoust. Soc. Amer.*, vol. 105, no. 6, pp. 3176–3184, Jun. 1999.
- [18] S. Kim, G. F. Edelmann, W. A. Kuperman, W. S. Hodgkiss, H. C. Song, and T. Akal, "Spatial resolution of time-reversal arrays in shallow water," *J. Acoust. Soc. Amer.*, vol. 110, no. 2, pp. 820–829, Aug. 2001.
- [19] I. T. Jolliffe, *Principal Component Analysis*, 2nd ed. New York: Springer-Verlag, 2002.
- [20] G. Bal and R. Verastegui, "Time reversal in changing environment," *Multiscale Model. Simul.*, vol. 2, no. 4, pp. 639–661, 2004.
- [21] A. Ishimaru, *Waves Propagation in Scattering and Random Media*. Piscataway, NJ: IEEE Press, 1999.
- [22] G. Bal and L. Ryzhik, "Time reversal and refocusing in random media," *SIAM J. Appl. Math.*, vol. 63, no. 5, pp. 1475–1498, 2003.



Dehong Liu (S'01–M'03) was born in Hubei, China, in 1975. He received the B.S., M.S., and Ph.D. degrees in electrical engineering from Tsinghua University, Beijing, China, in 1997, 1999, and 2002, respectively.

Since 2003, he has been working as a Research Associate with the Department of Electrical and Computer Engineering, Duke University, Durham, NC. His research interests include time reversal, array signal processing, short-pulse propagation modeling, and electromagnetic compatibility problems.



Jeffrey Krolik (S'82–M'83) received the Ph.D. degree in electrical engineering from the University of Toronto, Toronto, ON, Canada, in 1987.

He is currently a Professor of electrical and computer engineering with Duke University, Durham, NC. He has been with Concordia University, Montreal, and the University of California, San Diego, before coming to Duke in 1992. Since the time he joined Duke, he has broadened his research interests to include statistical signal processing for surveillance radars, as well as active and passive sonar. As a consultant, he has worked for the Defense Advanced Research Projects Agency, the Air Force Rome Laboratories, and the Office of Naval Research. He served as the Associate Editor of Acoustic Signal Processing for the *Journal of the Acoustical Society of America* from 1995–1998.

Dr. Krolik was awarded an IEEE Signal Processing Society Young Author Best Paper award in 1990 and was honored as a Duke University Yoh Faculty Scholar from 1993–1996. He is a founding member of the Sensor and Multichannel Signal Processing Technical Committee of the IEEE Signal Processing Society.

Lawrence Carin (S'86–M'89–SM'96–F'01) was born in Washington, DC, on March 25, 1963. He received the B.S., M.S., and Ph.D. degrees in electrical engineering from the University of Maryland, College Park, in 1985, 1986, and 1989, respectively.

In 1989, he joined the Electrical Engineering Department, Polytechnic University, Brooklyn, as an Assistant Professor and became an Associate Professor there in 1994. In September 1995, he joined the Electrical and Computer Engineering Department, Duke University, where he is now the William H. Younger Distinguished Professor. He has been the Principal Investigator on several large research programs, including two Multidisciplinary University Research Initiative programs. He is the cofounder of the small business Signal Innovations Group (SIG), which was purchased in 2006 by Integrian, Inc. He is the Director of Technology at SIG, which is now a subsidiary of Integrian. His current research interests include signal processing and machine learning for sensing applications.

Dr. Carin was an Associate Editor of the IEEE TRANSACTIONS ON ANTENNAS AND PROPAGATION from 1996–2001. He is a member of the Tau Beta Pi and Eta Kappa Nu honor societies.